Formation of polycrystalline TiO$_2$ on the ablated surfaces of RbTiOPO$_4$ single crystals by thermal annealing

J. J. Carvajal,*[a] G. Raj Kumar,[a] J. Massons,[a] J. R. Vázquez de Aldana,[b] I. Gallardo,[c] P. Moreno,[b] L. Roso,[c] F. Díaz[a] and M. Aguiló[a]

We investigated the structural effects that ultrafast laser ablation has on RbTiOPO$_4$ (RTP) single crystals. Raman scattering analysis revealed that a polycrystalline layer of RTP substituted the original material on the surface of the microstructured areas which is mainly responsible for the roughness observed in these structures. A later annealing treatment on the ablated samples resulted in the formation of a layer of sub-micrometric particles of TiO$_2$ in a mixed form of anatase and rutile, due to the decomposition of the polycrystalline RTP layer. This allows the development of engineering strategies to fabricate RTP–TiO$_2$ composites, with mixed properties, that might allow the combination of the non-linear optical properties of RTP and the light dispersive and electrical properties of TiO$_2$.

Introduction

Femtosecond lasers have become significant tools for micro-machining materials in order to fabricate photonic devices such as waveguides,[1] gratings,[2] or optical data storage systems,[3] among others. Ultrafast lasers provide extremely short, high intensity pulses which cause nonlinear photoionization effects and subsequent avalanche ionization that lead to the generation of a free-electron plasma in transparent dielectrics. When the density of the free electrons exceeds a certain threshold, absorbed energy is enough to produce macroscopic ablation.[4] The advantages of ultrafast laser ablation compared with other micromachining techniques, such as mechanical machining, electron- or ion-beam patterning and lithographic techniques, are that surface modification, such as relief formation, or modification of refractive indices in transparent solids is not linked to thermal collateral effects, it works at a high speed and it is a non-contact technique.[5] Thus, femtosecond laser ablation has become increasingly important in the last few years owing to the large amount of practical applications and the variety of materials that can be processed, including surface modification of metals,[6] polymers,[7] semiconductors,[8] and transparent materials.[9] Particularly, ultrafast laser ablation is a very promising method for the micro-structuration of wide bandgap or hard dielectric materials which is difficult to obtain by using other techniques.[10,11]

Nonlinear optical materials are highly attractive targets for femtosecond laser processing because of their nonvanishing nonlinear optical susceptibility $\chi^{(2)}$ modulation, so that they can be used in frequency conversion for potential applications in photonics.[12] These microstructured nonlinear optical materials could provide simultaneous control over the intensity, wavelength and spatial distribution of the generated frequency.[13] Up to now, a few studies have been devoted to investigate these effects in nonlinear optical materials such as KH$_2$PO$_4$ (KDP),[12] LiNbO$_3$,[14] β-BaB$_2$O$_4$,[15,16] LiTaO$_3$,[17] and more recently RbTiOPO$_4$ (RTP)[18] micro-structured by ultrafast laser ablation. In such integrated self-diffracting nonlinear crystals, it has been reported that multiple non-collinear second harmonic beams and controlled non-collinear fundamental laser beam propagation can be achieved without the requirement of additional elements such as external diffraction gratings or beam splitters. The micro-structured nonlinear optical materials could extend their possibilities as multi-frequency self-converter systems particularly in the field of telecommunications.

However, ultrafast laser ablation can also induce structural stress in these materials that might affect their properties. During femtosecond irradiation, very high transient temperatures in the electron subsystem are induced. Moreover, the electron pressure can become dominant over the elastic pressure, initiating material expansion, so that when the pressure force is stronger than the binding force, material ejection occurs. Although ablation only takes place in the region where the beam has been tightly focused, the surrounding material

[a] *Física i Cristal·lografia de Materials i Nano materials (FiCMA-FiCNA), Universitat Rovira i Virgili (URV), Campus Sescelades, Marcel·lí Domingo s/n, Tarragona, E-43007, Spain. E-mail: joanjosep.carvajal@urv.cat; Fax: +34 977 55 9563; Tel: +34 977 55 8790*
[b] *Grupo de Microprocesado de Materiales con Láser, Universidad de Salamanca, Pl. La Merced s/n, Salamanca, E-37008, Spain*
[c] *Centro de Láseres Pulsados (CLPU), C/Adaja s/n, Edificio M3, Villamayor, Salamanca, E-37185, Spain*

is affected by the shock waves generated in the ablation region. These shock waves can induce permanent microstructural modifications that can result in internal and/or surface stress of the material.[19,20]

The stress and structural changes generated in a material can be investigated by Raman scattering,[21] among other techniques. Raman scattering has proven to be a very efficient technique for structural characterization of materials, mainly because it is non-destructive, easy to implement, fast and does not require sample preparation.[22] The Raman scattered light contains information about the atomic lattice vibrations (phonons) that are selectively modified when the material is submitted to a mechanical stress. Thus, Raman scattering helps to obtain a quantitative description of the spatial distribution of the shock wave induced permanent stress under different conditions such as pulse length and pulse energy, providing additional information about the light–matter interaction during the ablation process.[19] This makes Raman scattering one of the most effective tools for strain determination in a wide range of materials. By using micro-Raman (μ-Raman) scattering, we can establish a map of strain in the irradiated structures with a spatial resolution down to the submicrometer scale.[23,24]

RTP belongs to the large family of isostructural compounds to $KTiOPO_4$ that crystallize in the orthorhombic system with the $Pna2_1$ space group of symmetry.[25] These crystals are well known due to their excellent nonlinear optical properties.[26,27] The linear and nonlinear optical properties of RTP crystals are very similar to those of KTP,[28] but they are more preferable in some practical applications, such as high repetition rate electro-optical modulators,[29] and applications that benefit from the higher laser damage threshold of RTP as compared to KTP.[30]

In this paper, we characterized the effects that ultrafast laser ablation, under different processing conditions, generates on the surface of RTP single crystals using μ-Raman scattering. A layer of polycrystalline RTP has been observed in the structures generated on the surface of RTP single crystals, creating a rough surface on the ablated areas. By thermal annealing, this polycrystalline RTP layer was transformed into polycrystalline TiO_2 in the form of anatase, although a small part of rutile was observed as well.

Experimental techniques

Crystal growth

RTP melts incongruently at 1443 K, so it cannot be grown by melting methods and it has been traditionally grown by high temperature solution techniques, such as the Top-Seeded Solution Growth (TSSG) method.[31] Around 140 g of solution were prepared in a platinum cylindrical crucible of 125 cm^3 by mixing the desired ratios of the corresponding oxides ($Rb_2O–TiO_2–P_2O_5–WO_3$ = 42.24–16.80–18.96–20 mol%). The crystals were grown from WO_3 containing fluxes to reduce the viscosity of the solution during the growth process.[32] The solution was homogenized at 50–100 K above the crystallization temperature. RTP crystals were grown on c-oriented crystal

seeds. We determined the saturation temperature of the solution by observing the growth or dissolution of the crystalline seed in contact with the surface of the solution. During the growth, the crystal seed was rotated at an angular speed of 45 rpm. We decreased the temperature of the solution by 20 K from the saturation temperature at a cooling rate of 0.1 K h^{-1} to activate the growth process. At the end of the crystal growth process, the crystal was completely extracted from the solution and slowly cooled to room temperature inside the furnace.

Preparation of samples for microstructuration

To prepare the samples for microstructuring by ultrafast laser ablation, the single crystals were cut and polished in a crystallographically oriented manner. First, the samples were cut with the correct crystallographic orientation to obtain a surface perpendicular to the c-crystallographic direction by placing them on a goniometer coupled to a Struers Accutom-50 diamond saw. As a reference to correctly orient the crystals, we used their morphology. Finally, the samples were polished in a Logitech PM5 polisher with an oscillatory arm. This enables one to accurately rotate and pressurize the samples depending on the hardness of the material to be polished. As abrasive substances, alumina powders with a grain size of 9, 3, 1, and 0.3 μm were used sequentially. At the end of the process, we verified the correct crystallographic orientation of the sample by X-ray diffraction using a Bruker-AXS D8-Discover diffractometer equipped with a parallel incident beam (Göbel mirror), a vertical θ–θ goniometer, an XYZ motorized stage and a General Area Diffraction Detection System (GADDS) HI-STAR detector. For the measurements, we used Cu Kα radiation. The X-ray diffractometer was operated at 40 kV and 10 mA. We collected 2D X-ray diffraction patterns covering a range of 2θ between 5 and 85° at a distance of 15 cm from the sample. The exposure time was 10 s per frame.

A Sensofar PLμ 2300 interferometric confocal microscope working as an optical profiler and an auto-collimator were used to measure the quality of the polishing using parameters such as roughness, flatness and parallelism between opposite faces of the sample. Under these conditions, we fabricated a sample with a surface of 4 × 3 mm^2 perpendicular to the c-crystallographic direction, with a mean roughness of 50 nm and a flatness radius of 14 m.

Ultrafast laser ablation

Two different arrays of channels have been fabricated on the (001) surface of RTP single crystals by ultrafast laser ablation using a commercial Ti : sapphire oscillator (Tsunami, Spectra Physics) and a regenerative amplifier system (Spitfire, Spectra Physics) based on chirped pulsed amplification (CPA). The laser system delivers linearly polarized 120 fs pulses with a central wavelength of 795 nm and a repetition rate of 1 kHz. The transverse mode of the beam was nearly TEM_{00} and the width was 9 mm (1 e^{-2} criterion).

The RTP samples were placed on a motorized XYZ translation stage that allowed achievement of optimal focusing on

the target surface, with the (001) face of the samples perpendicular to the laser beam propagation. The ablation threshold fluence depends on the number of pulses per spot, resulting in 1.44 ± 0.18 J cm^{-2} for 40 pulses and decreasing to 1.18 ± 0.15 J cm^{-2} for a larger number of pulses (>100 pulses) giving an incubation factor ξ = 0.783.[33,34] The laser beam was focused by means of a 50 mm achromatic lens onto the sample with pulse energies of 0.27–0.78 μJ, which provided peak fluences of 3.2–6.1 cm^{-2} at focus. The sample was moved following straight lines parallel to the b crystallographic axis and all across the surface, at constant scanning speeds of 75–130 μm s^{-1}, avoiding the iterative passes along the same line, depending on the depth and width of the features desired to write on the surface of RTP.[18] For those scanning speeds and the focusing conditions used, the number of pulses contributing to the ablation of a point within the sample surface was 40–55, thus the peak fluence used was well above the threshold fluence.

Fig. 1 presents the top and lateral views of the grooves inscribed in RTP samples by ultrafast laser ablation. The width and depth of the grooves depended on the ablation parameters used, such as laser fluence, pulse energy and focusing conditions of the laser beam. The lateral views of the grooves show that these structures present a V-shape.

Thermal annealing

A thermal treatment process, consisting of a heating step from ambient temperature to 1173 K at a heating rate of 15 K h^{-1}, a thermalization step at 1173 K for 5 h, and finally a cooling step to room temperature at 15 K h^{-1}, to avoid thermal stresses in the sample, was carried out on the RTP sample after the ultrafast laser ablation process. This was done to analyze the possibilities of thermal treatment to smooth the roughness generated by the ultrafast laser ablation process and, at the same time, analyze the possibilities of removing the polycrystalline layer of RTP formed during the ablation process.

Micro-Raman scattering

Micro-Raman (μ-Raman) scattering was used to analyze the effects of ultrafast laser ablation on the structure of RTP.

μ-Raman scattering measurements were carried out using a μ-Raman system Renishaw confocal InVia spectrometer equipped with a confocal microscope Leica 2500 and a CCD camera as a detector. The radiation of an Ar laser (λ = 514 nm and 25 mW) was focused by a 100× long working distance microscope objective on the surface of the samples. A back scattering scheme was used to detect the Raman signal through a confocal hole, allowing the extraction of the light scattered from an extremely small region of the sample with a resolution of about 0.5 μm. Approximately 75 measurements were recorded for each sample along the surface, edge, and depth of the channels.

Results and discussion

Characterization of the ablated samples

A complete analysis of the possible structural modifications in the ablated areas of the samples was carried out by recording μ-Raman spectra at the ablated and raw regions of the crystals. The results obtained are shown in Fig. 2, where we have plotted the spectra as a function of the distance along the surface covering ablated and non-ablated areas, recorded in the direction perpendicular to the grooves. From the figure, the existence of a change in the intensity of some Raman peaks from the ablated areas to the raw surface is clear.

A more detailed study of the differences among the recorded spectra is shown in Fig. 3(a). Two different spectra were observed, one corresponding to the ablated areas and the other one corresponding to the non-ablated areas. The main differences between them are the change in the intensity of the peaks located at 758 cm^{-1} and 978 cm^{-1} that decrease in the ablated areas, whereas the peak located at 693 cm^{-1} increases its intensity in the same areas.

The Raman spectra features of these materials are predominantly due to the vibrational motions of the TiO$_6$ octahedra and the PO$_4$ tetrahedra.[35] The regions from 200 to 400 cm^{-1} and from 600 to 800 cm^{-1} are associated with torsional and stretching vibrational modes of the TiO$_6$ octahedra, respectively. The Raman bands in the 850–1200 cm^{-1} region are due to the three degenerate modes of the PO$_4$ tetrahedra. Below 100 cm^{-1}, we can observe modes related to
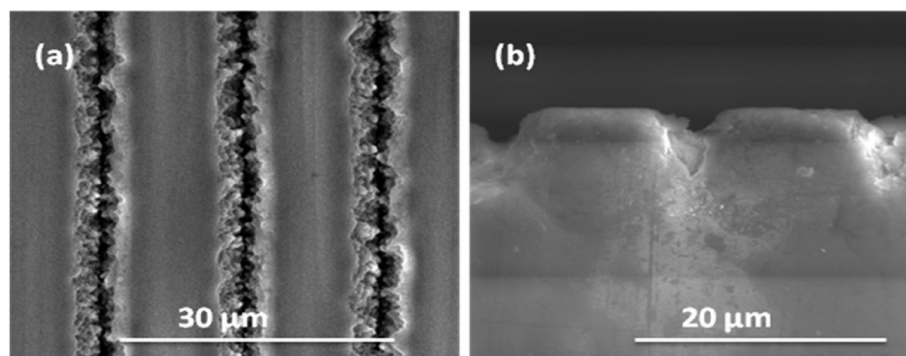

Fig. 1   SEM images of the grooves inscribed by ultrafast laser ablation on the (001) surface of RTP single crystals: (a) top and (b) lateral views.
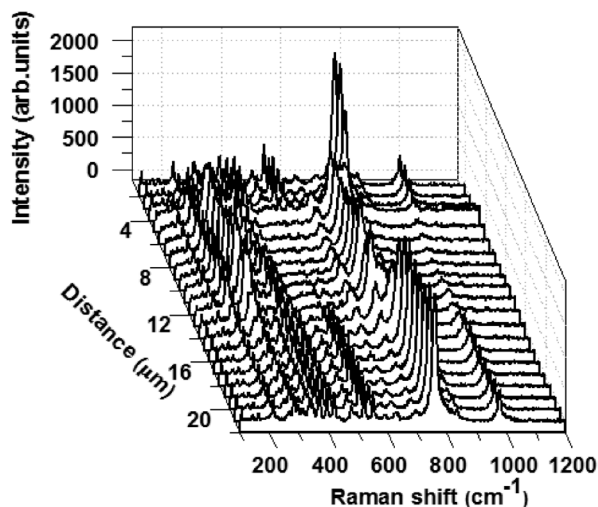
Fig. 2 3D plot of Raman spectra as a function of the distance along the surface, covering ablated and non-ablated areas of the RTP samples.

Rb–O polar vibrations and translational modes of Rb ions.[35] Thus, the changes observed in the spectra affect all the molecular groups involved in the RTP crystals.

The spectrum observed for the non-ablated regions is similar to that recorded in a polarized $z(yy)\bar{z}$ configuration of the RTP crystal,[36] as can be seen in Fig. 3(b), despite being recorded in a non-polarized configuration, which would explain the discrepancies between these two spectra. On the

other hand, we observed that the spectra recorded at the ablated regions coincide with that of the polycrystalline RTP. Fig. 3(c) shows the comparison of the Raman spectrum recorded for powdered RTP and the Raman spectrum of the ablated regions in the single crystals. This result would indicate the formation of polycrystalline RTP in the ablated areas that might be related with the redeposition of the material after the ablation process. This polycrystalline layer of RTP on the surface could be formed by sublimation of the material and fast condensation on the surface of the single crystal, although some contribution to its formation could also be expected from the mechanical detachment of the surface material resulting in shock wave propagation. During the ablation process, we observed the ejection of high quantities of material that can be deposited on the surface of the sample as debris. This polycrystalline layer could be part of the debris formed during the ablation process, but it is strongly attached to the surface of the grooves and could not be removed by mechanical means.

However, the most interesting aspect here is the mechanism of formation of this layer of polycrystalline RTP. As we commented in the experimental section, RTP melts incongruently, i.e. it decomposes before melting.[37] Thus, the formation of polycrystalline RTP could not be explained in terms of melting of the material and later solidification. Instead, the high energy provided during the ultrafast laser ablation of RTP can directly sublimate the material that condensates later in colder parts of the single crystal. In fact, this is the
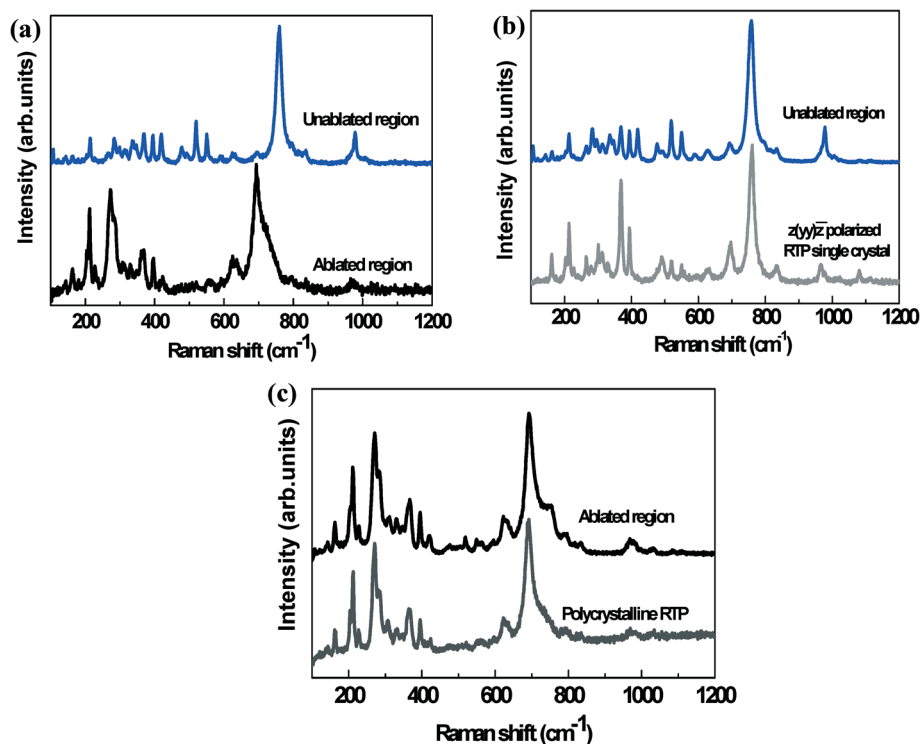

Fig. 3 (a) Raman spectra recorded at the ablated and non-ablated areas of the RTP sample. (b) Comparison of the Raman spectra recorded at the non-ablated areas with the $z(yy)\bar{z}$ polarized Raman spectra of RTP single crystals. (c) Comparison of the Raman spectra recorded at the ablated areas with the Raman spectra of polycrystalline RTP.

mechanism followed in the fabrication of nanoparticles of different materials by ultrafast laser ablation in a liquid environment.[38] This would be the first evidence that nanoparticles of RTP can also be formed by this mechanism, even when the material melts incongruently. In that case, since we do not use a liquid environment in which the nanoparticles can nucleate, they do it on the surface of the single crystal and they remain attached to it. This phenomenon, however, was not observed in other non-linear optical materials structured by the same technique.

As we can see in Fig. 2, the increase in intensity of the peak located at 693 cm^{-1}, that is one of the characteristic peaks of polycrystalline RTP, coincides with the decrease in intensity of the peak located at 758 cm^{-1}. Thus, the change in intensity of the peak located at 758 cm^{-1} in the ablated and non-ablated areas allowed us to establish a profile of the area on which the polycrystalline RTP layer has been deposited around the ablated area. Fig. 4(a) shows the intensity profile established by monitoring the change in intensity of the 758 cm^{-1} peak along 12 μm on the surface of the RTP sample covering ablated and non-ablated areas. As background in these graphs, we used a cross-sectional SEM image of the same area. As it can be seen in the image, there is an area affected by the ablation process at the surroundings of the grooves, around 1 μm wide at each side of the channel. This would indicate that there exists a layer of polycrystalline RTP with a thickness of ~1 μm at each side of the channel that has been deposited during the ablation process and that gives rise to the remarkable roughness observed at the edges of the grooves. Since Raman spectra were collected every 0.5 μm, this would coincide with the roughness determined from the SEM images recorded for this sample. Similar results were obtained when monitoring the change in intensity of the 693 cm^{-1} peak.

When we recorded the Raman spectra at different depths at the ablated and non-ablated areas, we observed a similar situation. Two different Raman spectra were again observed: (i) one corresponding to the ablated areas that matches the polycrystalline RTP spectrum and (ii) one corresponding to the non-ablated areas that coincided with the polarized Raman spectrum of RTP under the $z(yy)\bar{z}$ configuration.

Plotting again the variation of the intensity of the 758 cm^{-1} peak, we could establish a profile of the area in which we can detect the polycrystalline RTP deposited by the ultrafast laser ablation process and that was still attached to the crystal, as can be seen in Fig. 4(b).

Effects of thermal annealing on the ablated samples

We explored the possibilities of removing this polycrystalline layer of RTP and the possible internal stresses generated by the ultrafast laser ablation process on the RTP samples by performing thermal annealing on the sample.

Thermal annealing can result in a relief of internal stresses, softening, chemical homogenizing and transformation of the grain structure into a more stable state. During thermal annealing, atoms can move to more stable positions in the crystal lattice even affecting the morphology of the final product.[39] Vacancies and interstitial defects can be eliminated and dislocations can be annihilated.[40] To explore the effects of thermal annealing on the samples, the RTP sample was annealed for 5 h at 1173 K. This temperature is below the decomposition of RTP.[37] Then, we recorded again the Raman scattering spectra at the ablated and non-ablated regions of the sample. The results are shown in Fig. 5(a).

When this figure is compared to Fig. 3(a), we can see that, while the spectra recorded at the non-ablated areas are similar, the spectra recorded at the ablated regions are completely different. The peak located at 693 cm^{-1} is still present after the annealing process, but it is not the most intense peak of the spectrum anymore. The most intense peak in the spectra is a new peak appearing at 142 cm^{-1}. By the way, several new peaks with medium intensities appear at 638, 515, 394, 272 and 211 cm^{-1}.

Thus, we have investigated whether a new phase has been formed during the annealing process on the surface of the ablated channels. In fact, the new peaks located at 638 cm^{-1}, 515 cm^{-1}, 394 cm^{-1} and 142 cm^{-1} correspond to the E_g, $A_{1g} + B_{1g}$, B_{1g}, and E_g Raman modes of TiO_2 in its anatase form.[41]

To confirm these results, we recorded X-ray diffraction patterns at this area using a micro-X-ray diffractometer equipped with a 500 μm collimator, allowing us to analyze
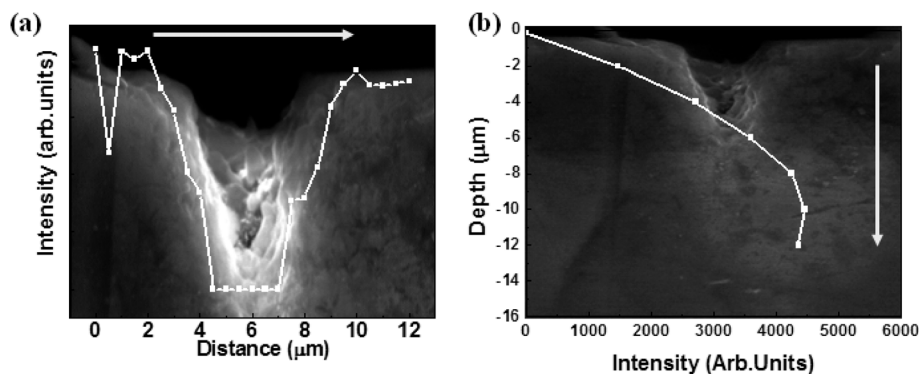

Fig. 4 Variation of the intensity of the Raman peak located at 758 cm^{-1} for RTP samples (a) along the surface and (b) along depth. Arrows indicate the direction of the measurement.
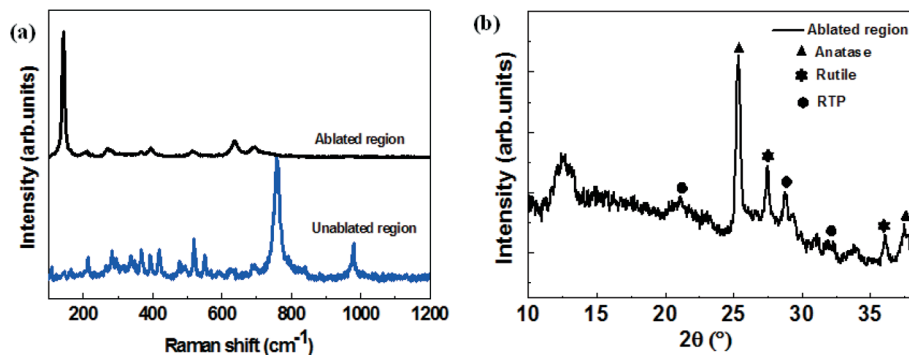
Fig. 5 (a) Raman spectra recorded at the ablated and non-ablated regions of the RTP sample after performing a thermal annealing treatment at 1173 K for 5 h. (b) X-ray diffraction pattern obtained on the surface of the RTP sample after an annealing treatment at 1173 K for 5 h. The peaks corresponding to the different phases, anatase, rutile and RTP, are shown with different symbols for a better identification of the crystalline phases present in the sample.

small regions of the sample. We recorded the diffraction pattern under specific conditions to avoid the diffraction of the (001) plane of the RTP substrate, and therefore maximizing the contributions from the polycrystalline layer on the surface of the channels. After integrating the diffraction pattern for more than 3 hours, we were able to record some peaks corresponding to one or more crystalline substances, as it can be seen in Fig. 5(b). We attributed these peaks to a mixture of TiO_2 in its forms of anatase and rutile, and a minor phase corresponding to polycrystalline RTP, according to the diffraction powder reference patterns for these substances from the JCPDS database: 00-021-1272 file for anatase, 01-086-0148 for rutile, and 01-072-3660 file for RTP.[42] The most intense peak corresponds to anatase, indicating that this is the major phase in the mixture, while RTP and rutile are present in lower quantities. The apparent discrepancy between the X-ray diffraction pattern and Raman spectra can be explained as a result of the weaker Raman signal of rutile as compared to that of anatase, which would not allow its detection in the Raman spectra. It has also been reported that the phase transition from anatase to rutile in TiO_2 nanoparticles evolves from the inner regions of the particles.[43] Thus, this effect would also mask the appearance of rutile in the Raman scattering.

The presence of TiO_2 is not surprising since it is one of the products formed during the decomposition of RTP.[37] However, RTP usually decomposes at temperatures above 1300 K. So far, it is surprising that RTP starts to decompose at a lower temperature (1173 K) in this case. This can be due to the incomplete bonds of the surface atoms, especially when the RTP grain sizes are in the submicrometer range, as it has been previously observed in the dewetting process of metal nanowires at much lower temperatures than their melting point.[39] Fig. 6 shows a SEM image of a channel inscribed on the RTP crystal after a chemical etching process with a mixture of $KOH:KNO_3$ (2:1 molar ratio) dissolved in water at 353 K during 15 min as well as a magnification of one of its walls. It reveals that grains with sizes around 100 nm constitute the distinctive feature within the surface of the channels. This would additionally support the hypothesis of the

reduction of decomposition temperature of polycrystalline RTP linked to the size of the crystalline grains. In fact, by applying the Scherrer equation[44] to the X-ray diffraction pattern recorded at the surface of the channels, we obtained an estimation of the size of the particles of 27 nm, supporting again that the reduction in the decomposition temperature of RTP is due to the size of the particles.

The stability of anatase is one point that should be considered as well. The phase transition in TiO_2 from anatase to rutile usually happens at temperatures around 1073 K.[45] However, in small-sized particles, surface free energy and stress play a crucial role in rendering the phase stability of anatase that, depending on the conditions, can be stable up to 1173 K, coexisting with rutile.[46] TiO_2 particles would have sizes ~28 nm in our case, as determined by the Scherrer equation, reinforcing this hypothesis. This size is also similar to the size of the RTP particles previously determined. Then, it seems possible that, as a result of the lower temperature for the decomposition of RTP in this case, we could stabilize the anatase phase, while in our previous studies,[37] we could only observe the formation of rutile, since RTP decomposed at much higher temperatures.

In that case, plotting the intensity of the peak appearing at 142 cm^{-1} in the Raman spectra allowed us to analyze the
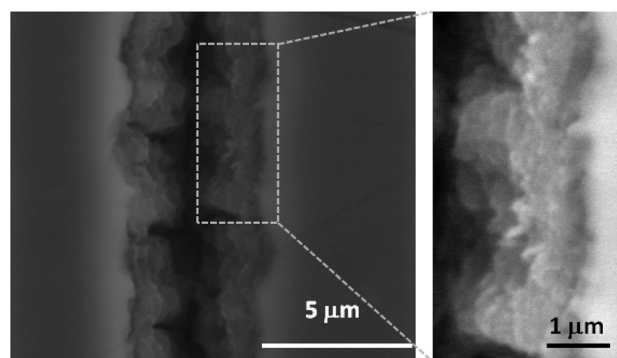

Fig. 6 SEM image of the surface of one of the channels inscribed on the surface of RTP after the chemical etching process with $KOH:KNO_3$ to reveal the grain structure of the surface.
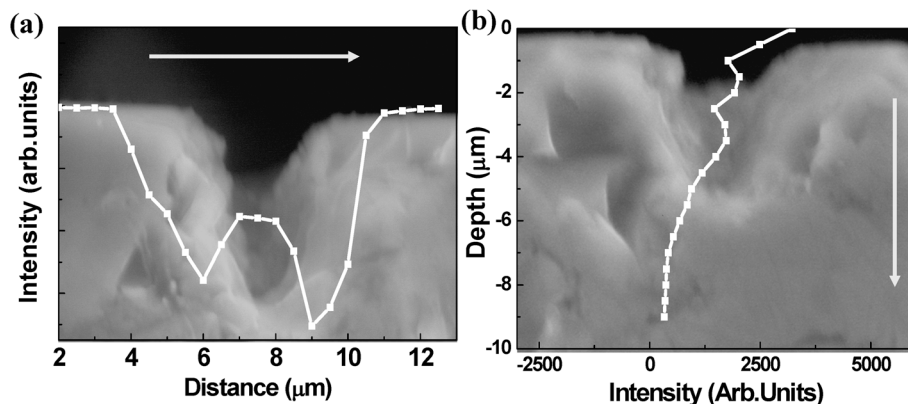
Fig. 7 Variation of the intensity of the Raman peak located at 142 cm^{-1} (a) along the surface and (b) along depth for the RTP sample. Arrows indicate the direction of the measurement.

thickness of the TiO_2 layer around the ablated and annealed grooves. Fig. 7(a) shows the difference in intensity of this peak along the surface of the RTP sample after annealing, covering ablated and non-ablated areas. Fig. 7(b) shows the same results but as a function of depth. In both cases, we added as background for these profiles a cross-sectional SEM image of the sample after annealing to provide a better comparison of the real width of the grooves and the thickness of the TiO_2 layer surrounding them.

In Fig. 7, we observed that the width of the channels from the recorded profiles from the Raman scattering spectra is again larger than the width of the channels determined by the SEM images. The profile obtained by Raman scattering is 0.75 μm wider at each side of the channel. This width is larger than that observed for the crystalline RTP layer (see Fig. 4), indicating that the polycrystalline RTP layer formed during the ultrafast laser ablation process was transformed to TiO_2 during the thermal annealing process. Additionally, a small layer of the RTP substrate surrounding the channel has also transformed into TiO_2. The cross-sectional SEM image recorded for the sample after the thermal annealing process reveals that the channels have a depth of around 6.5 μm, which would indicate that it would also increase during the thermal annealing process. According to the analysis of the profile obtained along the depth of the channels of the annealed sample by Raman scattering, there exists a layer of TiO_2 of ~2 μm below the channels. Comparing these results with those previously obtained on the annealed raw sample, this would indicate that only part of the polycrystalline RTP layer at the bottom of the channel decomposed to form TiO_2, which would also explain why we still observed polycrystalline RTP in the X-ray diffraction pattern of this sample.

Conclusions

We have shown that ultrafast laser ablation of the surface of RTP crystals causes the ablation of the material in a way that a polycrystalline layer of RTP appears on the ablated surfaces, roughening the surface of the grooves. This RTP polycrystalline layer is exclusively generated on the ablated areas, which

provides a tool to deposit selectively this polycrystalline layer on top of the substrate.

The groove roughness and the material modifications that take place during ultrafast ablation are crucial parameters in the performance of other photonic devices such as ridge optical waveguides,[47–49] affecting to their propagation losses, mode profiles, efficiencies in frequency conversion and laser action.

A post-annealing treatment of the sample at relatively high temperatures generated a polycrystalline layer of TiO_2 in its anatase form, formed by the thermal decomposition of polycrystalline RTP. This happens at a lower temperature than the reported decomposition temperature for bulk RTP, due to the nanodimensions of the grains of polycrystalline RTP.

Since TiO_2 nanoparticles have interesting properties as light scatterers, they might be used to enhance the diffraction properties of these structured RTP crystals. Also, as TiO_2 anatase–rutile composites are used as catalysts for generating hydrogen from water under UV-visible light illumination,[43] these new RTP–TiO_2 composites might find interest in generating hydrogen from water splitting under red or near-IR illumination and frequency conversion by the non-linear optical properties of RTP. Finally, another application of interest might be the use of TiO_2 as a transparent electrode for the generation of periodically poled RTP crystals by electrical poling,[50] in which the position of the electrodes can be defined by ultrafast laser ablation, instead of using the photolithography processes used up to now.

References

1 K. M. Davis, K. Miura, N. Sugimoto and K. Hirao, *Opt. Lett.*, 1996, **21**, 1729–1731.

2   L. Sudrie, M. Franco, B. Prade and A. Mysyrowicz, *Opt. Commun.*, 1999, **171**, 279–284.

3   E. N. Glezer, M. Milosavljevic, L. Huang, R. J. Finlay, T. H. Her, J. P. Callan and E. Mazur, *Opt. Lett.*, 1996, **21**, 2023–2025.

4   G. Dumitru, V. Romano, H. Weber, M. Sentis and W. Marine, *Appl. Phys. A: Mater. Sci. Process.*, 2002, **74**, 729–739.

5   M. D. Perry, B. C. Stuart, P. S. Banks, M. D. Feit, V. Yanovsky and A. M. Rubenchick, *J. Appl. Phys.*, 1999, **85**, 6803–6810.

6   M. Feuerhake, J. H. Klein-Wiele, G. Marowsky and P. Simon, *Appl. Phys. A: Mater. Sci. Process.*, 1998, **67**, 603–606.

7   S. Küper and M. Stuke, *Appl. Phys. Lett.*, 1999, **54**, 4–6.

8   G. Herbst, M. Steiner, G. Marowsky and E. Matthias, *Mater. Res. Soc. Symp. Proc.*, 1996, **397**, 69–75.

9   K. Kawamura, T. Ogawa, N. Sarukura, M. Hirano and H. Hosono, *Appl. Phys. B: Lasers Opt.*, 2000, **71**, 119–121.

10 I. H. Chowdhury, A. Q. Wu, X. Xu and A. Weiner, *Appl. Phys. A: Mater. Sci. Process.*, 2005, **81**, 1627–1632.

11 R. Gattass and E. Mazur, *Nat. Photonics*, 2008, **2**, 219–225.

12 B. Yu, P. Lu, N. Dai, Y. Li, X. Wang, Y. Wang and Q. Zheng, *J. Opt. A: Pure Appl. Opt.*, 2008, **10**, 035301.

13 C. Mendez, J. R. Vazquez de Aldana, G. A. Torchia and L. Roso, *Opt. Lett.*, 2005, **30**, 2763–2765.

14 G. A. Torchia, C. Mendez, I. Arias, L. Roso, A. Rodenas and D. Jaque, *Appl. Phys. B: Lasers Opt.*, 2006, **83**, 559–563.

15 Y. Li, P. Lu, N. Dai, X. Wang, Y. Wang, B. Yu and H. Long, *Appl. Phys. B: Lasers Opt.*, 2007, **88**, 227–230.

16 C. Romero, J. R. Vázquez de Aldana, C. Méndez and L. Roso, *Opt. Express*, 2008, **16**, 18109–18117.

17 Y. Zhang, X. Chen, H. Chen and Y. Xia, *Appl. Surf. Sci.*, 2007, **253**, 8874–8878.

18 G. Raj Kumar, J. J. Carvajal, M. C. Pujol, X. Mateos, J. Grau, J. Massons, J. R. Vázquez de Aldana, C. Mendez, P. Moreno, L. Roso, J. Ferre-Borrull, J. Pallares, L. F. Marsal, M. Aguiló and F. Díaz, *Opt. Mater.*, 2011, **34**, 207–214.

19 A. Rodenas, J. A. Sanz García, D. Jaque, G. A. Torchia, C. Mendez, I. Arias, L. Roso and F. Agulló-Rueda, *J. Appl. Phys.*, 2006, **100**, 033521.

20 J. Lamela, D. Jaque, A. Rodenas, F. Jaque, G. A. Torchia, J. R. Vázquez de Aldana, C. Méndez and L. Roso, *Appl. Phys. A: Mater. Sci. Process.*, 2008, **93**, 177–181.

21 R. Ossikovski, Q. Nguyen, G. Picardi and J. Schreiber, *J. Appl. Phys.*, 2008, **103**, 93525.

22 W. H. Weber and R. Merlin, Raman Scattering in Material Science, *Springer Series in Materials Science*, Springer, Berlin, 2000, vol. 42.

23 F. Dombrowski, I. De Wolf and B. Dietrich, *Appl. Phys. Lett.*, 1999, **75**, 2450–2452.

24 V. Poborchii, T. Tada and T. Kanayama, *Appl. Phys. Lett.*, 2006, **89**, 233505.

25 P. A. Thomas, S. C. Mayo and B. E. Watts, *Acta Crystallogr., Sect. B: Struct. Sci.*, 1992, **48**, 401–407.

26 R. Masse and J. C. Grenier, *Bull. Soc. Fr. Mineral. Cristallogr.*, 1971, **94**, 437.

27 G. D. Stucky, M. L. F. Phillips and T. E. Gier, *Chem. Mater.*, 1989, **1**, 492–509.

28 M. V. Pack, D. J. Armstrong and A. V. Smith, *Appl. Opt.*, 2004, **43**, 3319–3323.

29 K. Nawata, M. Okida, K. Furuki and T. Omatsu, *Opt. Express*, 2007, **15**, 9123–9128.

30 Y. S. Oseledchik, S. P. Belokrys, V. V. Osadchuk, A. L. Prosvirnin, A. F. Selevich, V. V. Starshenko and K. V. Kuzemchenko, *J. Cryst. Growth*, 1992, **125**, 639–643.

31 J. J. Carvajal, R. Solé, J. Gavaldà, J. Massons, M. Rico, C. Zaldo, M. Aguiló and F. Díaz, *J. Alloys Compd.*, 2001, **323–324**, 231–235.

32 J. J. Carvajal, V. Nikolov, R. Solé, J. Gavaldà, J. Massons, M. Rico, C. Zaldo, M. Aguiló and F. Díaz, *Chem. Mater.*, 2000, **12**, 3171–3180.

33 S. Baudach, J. Bonse, J. Kruger and W. Kautek, *Appl. Surf. Sci.*, 2000, **154–155**, 555–560.

34 J. R. Vázquez de Aldana, C. Mendez and L. Roso, *Opt. Express*, 2006, **14**, 1329–1338.

35 G. E. Kugel, F. Bréhat, B. Wyncke, M. D. Fontana, G. Marnier, C. Carabatos-Nedelec and J. Mangin, *J. Phys. Chem.*, 1988, **21**, 5565.

36 J. J. Carvajal, P. Segonds, A. Peña, J. Zaccaro, B. Boulanger, F. Díaz and M. Aguiló, *J. Phys.: Condens. Matter*, 2007, **19**, 116214.

37 J. J. Carvajal, R. Solé, J. Gavaldà, J. Massons, F. Díaz and M. Aguiló, *Chem. Mater.*, 2003, **15**, 2730–2736.

38 M. Galceran, M. C. Pujol, C. Méndez, A. García, P. Moreno, L. Roso, M. Aguilo and F. Diaz, *J. Nanopart. Res.*, 2009, **11**, 717–724.

39 X. H. Huang, Z. Y. Zhan, X. Wang, Z. Zhang, G. Z. Xing, D. L. Guo, D. P. Leusink, L. X. Zheng and T. Wu, *Appl. Phys. Lett.*, 2010, **97**, 203112.

40 X. H. Huang, Z. Y. Zhan, K. P. Pramoda, C. Zhang, L. X. Zhang and S. J. Chua, *CrystEngComm*, 2012, **14**, 5164–5165.

41 J. Zhang, M. Li, Z. Feng, J. Chen and C. Li, *J. Phys. Chem. B*, 2006, **110**, 927–935.

42 Powder Diffraction File Database PDF-2, Joint Committee of Powder Diffraction Standards, JCPDS, 2011.

43 T. Cia, N. Li, Y. Zhang, M. B. Kruger, J. Murowchick, A. Selloni and X. Chen, *ACS Appl. Mater. Interfaces*, 2013, **5**, 9883–9890.

44 Y. Huang, X. F. Duan, Q. Q. Wei and C. M. Lieber, *Science*, 2001, **291**, 630–633.

45 P. S. Ha, H. J. Youn, H. S. Jung, K. S. Hong, Y. H. Park and K. H. Ko, *J. Colloid Interface Sci.*, 2000, **223**, 16–20.

46 Y. Djaoued, S. Badilescu, P. V. Ashrit, D. Bersani, P. P. Lottici and J. Robichaud, *J. Sol-Gel Sci. Technol.*, 2002, **24**, 255–264.

47 R. Degl'Innocenti, S. Reidt, A. Guarina, D. Rezzonico, G. Poberaj and P. Gunter, *J. Appl. Phys.*, 2006, **100**, 113121.

48 Y. Jia, N. Dong, F. Chen, J. R. Vázquez de Aldana, S. Akhmaladiev and S. Zhou, *Opt. Express*, 2012, **20**, 9763–9768.

49 Z. Bi, L. Wang, X. Liu, S. Zhang, M. Dong, Q. Zhao, X. Wu and K. Wang, *Opt. Express*, 2012, **20**, 6712–6719.

50 H. Karlsson, F. Laurell and L. K. Cheng, *Appl. Phys. Lett.*, 1999, **74**, 1519–1521.